Key Points:
- Effective diffusion coefficients are important to assess mineral reaction rates or transport in low-permeability rocks
- Effective diffusion coefficients can be predicted using fractal dimensions
- Fractal dimensions can be obtained using small-angle neutron scattering data

Correspondence to:
A. Busch,
a.busch@hw.ac.uk

Predicting Effective Diffusion Coefficients in Mudrocks Using a Fractal Model and Small-Angle Neutron Scattering Measurements

A. Busch[1] (ID), N. Kampman[2], P. Bertier[3] (ID), V. Pipich[4], A. Feoktystov[4], G. Rother[5] (ID), J. Harrington[6] (ID), L. Leu[7], M. Aertens[8], and E. Jacops[8]

[1]Heriot-Watt University, The Lyell Centre, Research Avenue South, Edinburgh, UK, [2]Shell Global Solutions International B.V., Rijswijk, The Netherlands, [3]Clay and Interface Mineralogy, RWTH Aachen University, Aachen, Germany, [4]Forschungszentrum Jülich GmbH (Jülich Centre for Neutron Science, JCNS) at Heinz Maier-Leibnitz Zentrum (MLZ), Garching, Germany, [5]Chemical Sciences Division, Oak Ridge National Laboratory, Oak Ridge, TN, USA, [6]Environmental Science Centre, Keyworth, British Geological Survey, Nottingham, UK, [7]Department of Earth Science and Engineering, Imperial College London, London, UK, [8]Belgian Nuclear Research Centre (SCK-CEN), Mol, Belgium

Abstract The determination of effective diffusion coefficients of gases or solutes in the water-saturated pore space of mudrocks is time consuming and technically challenging. Yet reliable values of effective diffusion coefficients are important to predict migration of hydrocarbon gases in unconventional reservoirs, dissipation of (explosive) gases through clay barriers in radioactive waste repositories, mineral alteration of seals to geological CO_2 storage reservoirs, and contaminant migration through aquitards. In this study, small-angle and very small angle neutron scattering techniques have been utilized to determine a range of transport properties in mudrocks, including porosity, pore size distributions, and surface and volume fractal dimensions of pores and grains, from which diffusive transport parameters can be estimated. Using a fractal model derived from Archie's law, we calculate effective diffusion coefficients from these parameters and compare them to laboratory-derived effective diffusion coefficients for CO_2, H_2, CH_4, and HTO on either the same or related mudrock samples. The samples include Opalinus Shale from the underground laboratory in Mont Terri, Switzerland, Boom Clay from a core drilled in Mol, Belgium, and a marine claystone cored in Utah, USA. The predicted values were compared to laboratory diffusion measurements. The measured and modeled diffusion coefficients show good agreement, differing generally by less than factor 5. Neutron or X-ray scattering analysis is therefore proposed as a novel method for fast, accurate estimation of effective diffusion coefficients in mudrocks, together with simultaneous measurement of multiple transport parameters including porosity, pore size distributions, and surface areas, important for (reactive) transport modeling.

1. Introduction

Molecular diffusion is the dominant transport mechanism in low-permeability sedimentary rocks, controlling fluid mobility on vast scales, regional diagenesis, reservoir seal capacity, source rock potential, and production from tight gas reservoirs. Early studies on molecular diffusion in geosystems focused on diffusional leakage of natural gas from reservoirs via the caprock (Krooss, 1988; Krooss & Schaefer, 1987; Leythaeuser et al.,1980), providing insight into the significance of this process over geological timescales. Subsequently, experimental studies have broadened to include different argillaceous rocks and various gas species, such as CH_4, N_2, or CO_2 (Schlömer & Krooss, 1997, 2004). Diffusion of gases or solutes is also important for the disposal of radioactive waste in geological repositories (Altmann et al., 2012; Maes et al., 2004, 2008; Rebour et al., 1997; Rubel et al., 2002; Van Loon et al., 2003), where knowledge of diffusion of radionuclides and hydrogen is required to predict dispersion, pressure evolution, and long-term containment (Jacops et al., 2013, 2015a, 2015b).

For geological CO_2 storage, caprock diffusion has been studied: (i) as a leakage mechanism (Busch et al., 2008), demonstrating that diffusion is only relevant over geological timescales; (ii) as a controlling parameter for mineral reactions (Kampman et al., 2016); and (iii) as a rate-limiting mechanism for CO_2-induced swelling of clay minerals (Wentinck & Busch, 2017). For unconventional hydrocarbon reservoirs, CH_4 diffusion experiments in (partially) water-saturated gas shale samples are rare or absent, with some measurements

of diffusion coefficients using equilibration curves from gas sorption data (Yuan et al., 2014). Diffusion experiments are typically performed on sample plugs by creating a concentration gradient across the water-saturated sample. The effluent concentration is measured over time until a steady state is reached. However, this requires long measurement times of weeks to months and/or small sample sizes of ≪1-cm thickness due to the low diffusion coefficients in mudrocks.

In order to overcome the difficulty of time-intensive plug measurements (if plugs are even available), attempts have been made to relate the transport properties (such as pore network tortuosity) to the fractal dimensions of the aggregated mass, pore space, and pore surfaces in soils or mudrocks (Ahl & Niemeyer, 1989; Gimenez et al., 1997; Radlinski, 2006). The mass and pore structure of sedimentary rocks, like sandstone or mudrocks, have been shown to exhibit self-similar scaling relationships, within certain limits of scale (Krohn, 1988; Radlinski et al., 1999; Thompson, 1991). Mathematical fractals are constructed from an initial object by the application of a repeating generator pattern. Cumulative application of the repeating pattern n times can result in either accretion or reduction of the initiator, and the final fractal object exhibits a number-size scaling relationship

$$N(r) = \kappa r^{-D} \tag{1}$$

where $N(r)$ is the number of elements of length equal to r, κ is the number of initiators of unit length, and D is the fractal dimension, which describes the power law scaling. The nature of the initiator determines the dimensionality (e.g., line, surface, or volume). Mathematical fractals are described as deterministic fractals because the same operation is repeated at all scales, whereas natural materials, such as rocks, include randomness in the processes, which generate these patterns and are better described as statistical fractals. The fractal nature of a natural material can in part be tested by measurement of a repetitious property of that material with units of regular shape and different characteristic size, l. If the scaling of the property is fractal, the number of units of a certain characteristic size $N(l)$, is related to l according to equation (1) such that

$$N(l) \propto l^{-D} \tag{2}$$

and the fractal dimension of the measured property is related to its dimensionality by

$$N(l)l^{D_T} \propto l^{D_T - D} \tag{3}$$

where D_T is the topological dimension of the measuring units (D_T = 1, 2, and 3 for a line, surface, or volume, respectively). The minimum requirements for a natural material to be considered fractal are that it is nowhere differentiable, able to have a fractal dimension, poses statistical self-similarity, fine or detailed structure at arbitrary small scales and irregularity locally and globally such that it is not easily described by traditional Euclidean geometry (Falconer, 2004); the structure of sedimentary rocks is generally accepted to satisfy these criteria, over certain limits of scale. The fractal nature of sedimentary grains, pores, and grain surfaces arises from a variety of processes related to sedimentary transport, sorting, weathering, mineral dissolution, and crystal growth. For example, the porosity of clay rich rocks is fractal in part as a result of the nature of the growth kinetics of coalesced fractal aggregates during the flocculation of mineral particles during sedimentation (Meakin, 1991; Sterling Jr et al., 2005).

These different fractal dimensions can be used to characterize the geometry of a porous medium in relation to transport processes (Ghanbarian et al., 2017; Yang et al., 2014; Zhang et al., 2017). Data to compute fractal dimensions can be obtained from various techniques, for example, 2-D optical microscopy or 3-D fluid intrusion data such as N_2 or CO_2 low-pressure sorption, or from nondestructive particle-scanning methods, such as small-angle scattering using neutrons or X-rays. The small pore sizes of mudrocks generally limit imaging of the pore networks to high-resolution techniques such as X-ray tomography (Backeberg et al., 2017) or Focused Ion Beam Scanning Electron Microscopy (Keller et al.,2013). Small-angle neutron scattering (SANS) techniques afford the opportunity to study the pore structure of mudrocks using a technique that allows rapid measurement of porosity, pore size distribution, pore surface areas, and the fractal dimensions of the material in a single measurement (Radlinski & Hinde, 2002).

Laboratory measurements of pore structure are typically conducted at the core plug or thin section scale (centimeters to tens of centimeters), whereas transport at the field scale integrates properties and processes over greater distances (meters to kilometers). The transport properties that govern effective diffusion rates are pore network tortuosity and porosity. Laboratory measurements integrate small-scale heterogeneities

(i.e., at the scale of laminae or sedimentary structures). Such measurements are generally thought to be representative of matrix transport properties at large scales because these properties typically converge (i.e., reach uniformity) over scales of a few centimeters, as has been shown for soils (Anderson et al., 2000; Crawford et al., 1993; Crawford & Matsui, 1996). Larger-scale heterogeneities (i.e., at the bedding or unit scale) are not integrated by the laboratory measurements but are also generally demarked by sharp and/or contrasting properties (i.e., changes in facies), which can be characterized with discrete measurements, and the effects integrated via numerical simulations (Cui et al., 2009). Field-scale diffusive transport in low-permeability rocks may be scale dependent, but this is thought to be a result of fine fracture networks that lead to scale-dependent transport properties as a result of the hierarchical nature of fracture networks and an increase in the fracture-matrix interface with scale (Liu et al., 2007).

In this study, we compare a compilation of matrix effective diffusion coefficients for different solutes (CO_2, H_2, CH_4, and HTO) with a fractal model developed by Liu and coworkers (Liu et al., 2004; Liu & Nie, 2001). Data used originate partly from published literature and partly from new data presented here. We show that the effective diffusion coefficients can be successfully predicted based on measurements of the surface and volume fractal of the pore network using SANS, providing a new method to recover the transport properties of low-permeability rocks.

2. Samples

We study three sample sets from different locations, depositional environment, and age. Mineralogical and petrophysical data are provided in Table 1, an overview on the origin of the experimental diffusion and SANS data in Table 2. Quantitative mineralogical composition was analyzed by means of powder X-ray diffraction. Mineralogical compositions were quantified by Rietveld refinement (Ufer et al., 2008). Cation-exchange capacities of bulk materials were determined using the Cu-triethylenetetramine complex (Cu-Trien) method (Stanjek & Künkel, 2016). Full details on both methods have been published previously (Seemann et al., 2017; Zeelmaekers et al., 2015).

Generally, mechanical unloading of the samples after coring and sample dehydration is considered irrelevant in this specific study that addresses the pore space of relatively small samples.

2.1. Opalinus Shale

Opalinus Shale samples were obtained from the shaly facies of the Opalinus Clay formation at the Mont Terri underground rock laboratory, St. Ursanne, Switzerland. The Opalinus Clay was deposited in the Aalenain (Dogger-α, ca. 174 Ma) in a shallow marine setting of an epicontinental sea at water depths of around 10–30 m and is high in clay content (~65%), containing mainly illite and kaolinite. In Mont Terri, samples are currently at a depth of 230 m but underwent a maximum burial of about 1,350 m (Bossart & Thury, 2008). From an ~2-m core section, ~1-cm disks were cut in 10-cm intervals. From these disks, samples for neutron scattering measurements have been prepared for this study and other petrophysical properties and mineralogy have been published previously (Busch et al., 2017).

2.2. Carmel Claystone

This sample was obtained from a scientific drilling campaign near Green River, Utah. The geological setting and depositional environment has been described previously (Kampman et al., 2013, 2014, 2016). The Carmel Formation is a 50-m-thick sequence of complex, laterally gradational lithofacies, comprising interbedded red and gray shale and bedded gypsum, red and gray mudstone/siltstone, and fine-grained sandstone. These are interpreted as Mid-Jurassic marine sediments deposited in quiet, subtidal conditions under the influence of periodic hypersaline water and form a regional seal (Blakey et al., 1996). For the diffusion experiments using CO_2 as a solute we used a plug drilled from a depth of 180.7 m, which mainly consists of illite as the only clay type (36%), calcite (22%), quartz (20%), and minor fractions of K-feldspar, dolomite, and hematite.

2.3. Boom Clay

The Boom Clay samples were taken from the ON-Mol1 borehole, drilled in 1997, near Mol, Belgium (Jacops et al., 2017). Since their retrieval in 1997, the cores have been stored under anoxic conditions at 4 °C. More specifically, samples were sealed in PVC tubes and packed in aluminium-coated PE foil under vacuum. In

Table 1
Sample Mineralogy, Cation Exchange Capacity, and Total Organic Carbon Content for the Sample Set Used in This Study

Sample	Quartz	Albite	K-feldspar	Kaolinite	Mus + Illite+I/S	Smectite	Chlorite	Calcite	Dolomite	Siderite	Pyrite	Anatase	Anhydrite	Gypsum	Hematite	Total	TOC	CEC	SLD	Grain density	Porosity
								%										meq/ kg	10^{-6} A^{-2}	g/cm	-
Opalinus Shale																					
CCP 1	19.6	1.9	2.2	21.6	43.8		3.1	3.5	0.8	1.1	0.7		0.9	0.7		99.9	1.2	129.1	3.74	2.75	0.19
CCP 4	15.3	1.4	2.3	20.3	50.4		3.8	2.5	0.5	1.3	0.7		1.0	0.4		99.9	1.3	144.6	3.72	2.77	0.18
CCP 5	12.5	1.1	1.6	22.2	50.8		4.0	4.6	0.3	0.5	0.7		1.0	0.8		100.1	1.5	151.5	3.70	2.77	0.20
CCP 6	14.5	1.4	2.0	21.5	48.5		3.9	4.2	0.5	0.9	1.0		1.0	0.6		100.0	1.3	145.6	3.74	2.77	0.19
CCP 7	12.8	1.6	2.5	22.2	45.1		4.4	7.2	0.3	1.1	1.2		1.0	0.7		100.1	1.2	145.0	3.73	2.78	0.19
CCP 9	12.1	0.8	1.6	21.3	52.6		4.4	3.4	0.4	0.3	1.7		1.0	0.4		100.0	1.1	157.9	3.73	2.78	0.21
CCP 12	14.5	1.4	2.0	21.5	48.5		3.9	4.2	0.5	0.9	1.0		1.0	0.6		100.0	1.3	145.6	3.73	2.77	0.19
CCP 14	14.5	1.4	2.0	21.5	48.5		3.9	4.2	0.5	0.9	1.0		1.0	0.6		100.0	1.3	145.6	3.73	2.77	0.19
Carmel Shale																					
Carmel	20.9		12.3		36.3			22.1	7.3						1.3	100.2		n.a.	4.24	2.75	0.13
Boom Clay*																					
K4 (127b)	28.0	1.0	5.0	9.2	29.1	17.9	4.9	2.0	0.0		2.0	0.7		0.5		100.2	0.3	129.1	3.17	2.70	0.40
K10 (48a)	32.0	2.0	10.0	6.4	22.7	19.7	4.2	0.8	0.6		1.0	0.6		0.0		100.0	0.2	150.5	3.13	2.65	0.42
K11 (48a)	33.0	3.0	6.0	6.1	23.4	21.7	3.9	0.4	0.5		1.0	0.7		0.0		99.6	0.2	147.6	3.05	2.64	0.39
K2 (84b)	31.0	3.0	8.0	9.0	26.5	13.8	3.7	0.2	0.0		2.0	0.6		0.6		98.4	0.2	144.6	3.34	2.65	0.34
K9 (112a)	26.0	0.7	5.0	12.4	26.0	24.0	2.6	0.0	0.0		2.0	0.7		0.3		99.7	0.2	151.5	2.92	2.65	0.38

Table 2
Overview of Samples and Measurements and Origin of Data

Sample	Diffusion experiments	SANS experiments
Opalinus Shale	Literature data (Pearson et al., 2003)	Literature data by the same authors on different samples than diffusion data (Busch et al., 2017)
Boom Clay	Literature data (Jacops et al., 2017)	This study on the same samples used for diffusion experiments
Carmel Claystone	This study	This study on the same samples used for diffusion experiments

total, five samples have been used for the neutron measurements and compared to experimentally derived values from the same samples (Jacops et al., 2017). The Boom Clay is a marine sediment, which was deposited in the early Oligocene (Rupelian) at water depths between 50 and 100 m, under reducing conditions. Samples were recovered from a depth of 168 to 246 m (Jacops et al., 2017), while maximum burial depth was slightly deeper of about 30 m (Beerten et al., 2013). It consists of different lithological subunits; specifically, a rhythmic alteration of silty and more clay-rich layers has been observed, as well as organic-rich and carbonate-rich layers. Based on these lithological variations, the Boom Clay has been subdivided in four members: the Boeretang Member, the Putte Member, the Terhagen Member, and the Belsele-Waas Member. Samples used in this study originate from the Putte and Boeretang Members and are classified as clayey (K2, K9, and K4) and silty (K10 and K11). Diffusion experiments were performed perpendicular to the bedding, except for sample K4, which was oriented parallel to the bedding. The mineralogy is dominated by quartz and illite/smectite, with minor fractions of muscovite, kaolinite, and K-feldspar. Total clay content varies between 53% and 65%.

3. Methods

### 3.1. Diffusion Measurements on Sample Plugs

Diffusion coefficients for Opalinus Shale and Boom Clay are taken from the literature. Opalinus Shale samples used previously were not identical to the ones used in the neutron scattering experiments but are from the same (shaly) facies. Boom Clay samples used for diffusion and neutron scattering tests originate from the same material and are directly comparable. A new set of diffusion experiments was performed on the Carmel Claystone and will be presented and discussed in a later section. All diffusion tests are comparable in the sense that samples used are of similar size and from shallow depths of a few hundred meters. The formation temperatures are ~20 °C, and pore water salinity is below seawater for all samples. A variety of different diffusing species have been used in the experiments, including different gases (CO_2, CH_4, and He) and tritiated water (HTO). The experimental design also varies; however, the overarching principle of such tests of establishing a zero pressure gradient and only a concentration gradient for the diffusing species is given.

3.1.1. Opalinus Shale

Diffusion coefficients based on the (V) SANS data have been obtained from plugs cut parallel to bedding. Experimental diffusion measurements have been summarized previously and are mainly based on a study by van Loon (Van Loon et al., 2003). For these experiments, a radial diffusion approach was chosen, where the water-saturated sample plug (d = 25.4 mm, l = 11 mm) is placed between porous stainless steel plates in a triaxial cell. Diffusion experiments are performed using the so-called Pearson water with a salinity of ~9.4 g/L (Pearson et al., 2003). The samples were water saturated over several weeks using artificial formation waters. After saturation, circulating fluids were exchanged with fluids containing a tracer (HTO, $^{36}Cl^-$ and $^{125}I^-$), of which HTO is of interest for comparison with our model. In addition, different confining pressures have been applied (1 and 5 MPa) to test the effect of sample compressibility. The solute is introduced through a central hole (d = 6.7 mm). These are steady state experiments that directly determine the effective diffusion coefficient.

3.1.2. Boom Clay

Diffusion coefficients on Boom Clay samples were used from Jacops et al. (Jacops et al., 2017). The basis is the double through-diffusion technique for dissolved gases, in which two water reservoirs with dissolved gases are placed on opposite sides of a saturated test core (d = 80 mm, l = 30 mm). The Boom Clay core was sealed in a stainless steel diffusion cell (constant volume), but no additional confining pressure was applied. It was
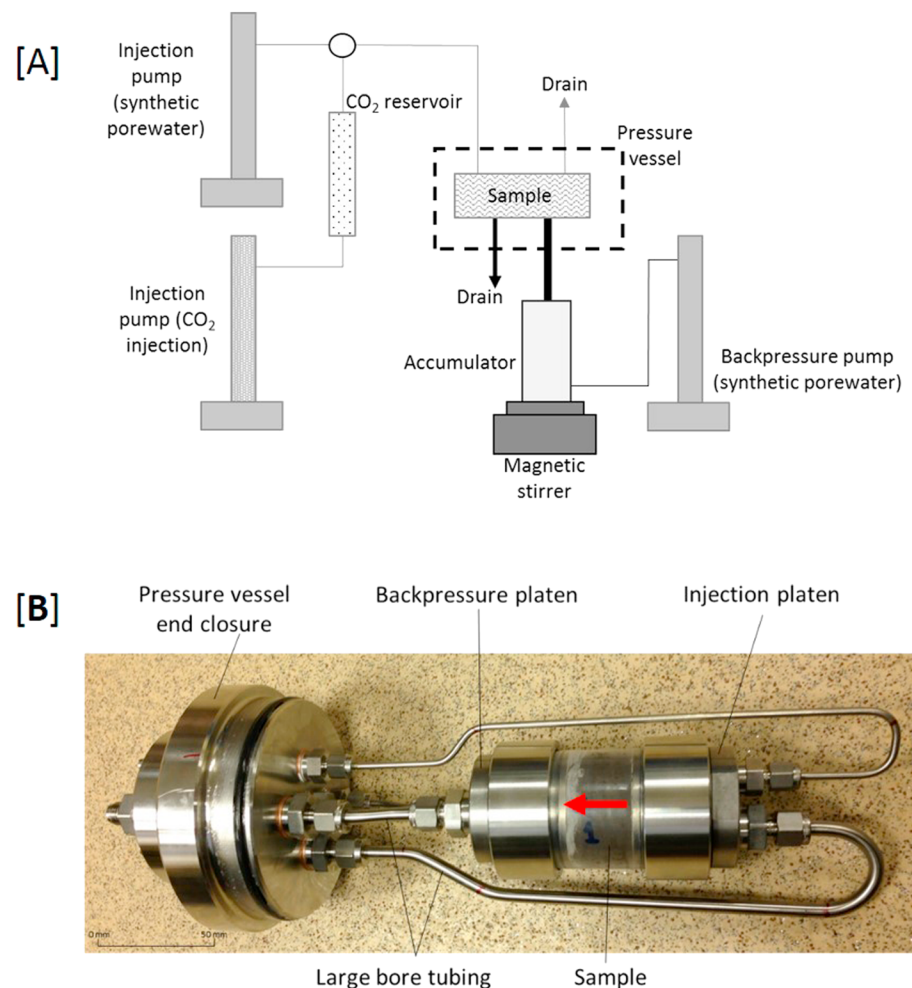
Figure 1. (a) Schematic showing configuration of apparatus. (b) Photo of diffusion cell assembly containing the Carmel sample. The red arrow marked on the sample denotes the direction of gas diffusion.

then connected via stainless steel filter plates to two water vessels containing oxygen-free synthetic pore water and 0.014 mol/L $NaHCO_3$ (salinity of 1.18 g/L) in order to mimic the composition of the Boom Clay pore water (De Craen et al., 2004). Both water vessels were pressurized, each with a different gas at the same total pressure (circa 500 ml gas at 1 MPa). In this way, no advective flux could occur and the clay sample remained fully water saturated. The waters at both sides were then circulated over the filters, which were in contact with the clay core, allowing the dissolved gases to diffuse through the clay core, toward the reservoir on the opposing side. The changes in gas composition in both reservoirs were measured as a function of time by gas chromatography. More information on the modeling of the gas and HTO diffusion experiments can be found in (Jacops et al., 2017).

3.1.3. Carmel Claystone

A CO_2 diffusion experiment was performed at the Transport Properties Research Laboratory, British Geological Survey. The basic permeameter (Figure 1) consists of five main components: (1) a sample assembly, (2) a 15-MPa rated pressure vessel and associated confining pressure system, (3) a fluid injection system, (4) a backpressure system, and (5) a PC-based data acquisition system. A large volume accumulator was placed at the downstream end of the system to maintain a fixed concentration gradient (Figure 1a) and placed on a magnetic stirring plate to promote mixing of the back-pressuring fluid, reducing the potential for solution gradients as the gas diffused into the downstream accumulator. To ensure that the apparatus performed as required, the system was modeled using existing data from Busch et al. (2008). This analysis was used to define the volume of the downstream accumulator.

Table 3
Sample Depth, Orientation, Stress Conditions, and Geotechnical Properties

Formation	Unit	Carmel
Depth	m	180.4–180.9
Orientation		Perpendicular to bedding
Injection pressure	MPa	2.0
Backpressure	MPa	2.0
Confining pressure	MPa	4.9
Moisture content	%	2.2
Dry density	g/cm^3	2.58
Bulk density	g/cm^3	2.63

Note. The parameters given should be considered as estimates because of the sensitivity of the calculated values to the very low porosity and moisture content of these materials.

The sample was sandwiched between two stainless steel end caps and jacketed in heat-shrink Teflon to exclude the confining fluid. The inlet and outlet zones for gas/water flow contained porous filter discs matched to the diameter of the sample. These acted as either source or sink for the injection of test permeants. Large diameter tubing (6.35-mm outer diameter) was used to connect inlet and outlet filters to their respective test systems.

To limit osmotic swelling of the specimen, a synthetic pore water solution was prepared for use as the back-pressuring fluid. Details of the hydrochemistry of the interstitial fluid were provided by Cambridge University, based on the in situ fluid sample DFS001 in contact with the caprock (Kampman et al., 2014). A stock solution with the following composition was used as the test fluid in all hydraulic and consolidation test stages: Ca^{2+} (25.31 mmol^{-1}); Mg^{2+} (10.54 ⊠mol^{-1}); Na^+ (52.58 mmol^{-1}); K^+ (5.17 mmol^{-1}); SO_4^{2-} (16.57 mmol^{-1}); Cl (33.60 mmol^{-1}); S_iO^{2+} (288.33 mol^{-1}); S_r^2 (119.70 mol^{-1}); Fe^{2+} (0.27 mol^{-1}); Mn^{2+} (103.84 mol^{-1}), Li^+ (0.07 mol^{-1}); $B+$ (0.10 mmol^{-1}); Al^{3+} (1.60 mol^{-1}); total salinity ~5 g/L; alkalinity 50.62 mEql^{-1}; pH (in situ) 5.30.

Prior to measuring the diffusion coefficient, the core was equilibrated under in situ conditions of effective stress to ensure that the sample was fully saturated and in equilibrium with the prevailing stress state. To measure the diffusion coefficient, CO_2 gas was placed in a reservoir connected to a second pump and allowed to equilibrate with the injection fluid prior to testing (Figure 1a). This ensured that the system was both leak tight and the pump fluids fully saturated with CO_2 prior to testing. Once complete, the injection pump was connected to the sample, and the intervening pore water flushed from the tube work to leave CO_2 in contact with the injection face of the sample. Pressure in each test circuit was maintained at a constant, zero differential pressure across the specimen. Fluxes in and out of the system were monitored over time to allow definition of the steady state diffusion coefficient. The key operational and sample properties are listed in Table 3.

Data in Figure 2 show cumulative CO_2 inflow for the Carmel test sample. The rate of transfer of CO_2 through the sample can be obtained from the slope of the cumulative flux response. According to Fick's law, the rate of transfer is given by

$$\text{Rate}\left[\frac{\text{mol}}{s}\right] = \frac{AD_e\Delta c}{L} \tag{4}$$

where A is the sample area (m^2), D_e is the effective diffusion coefficient (m^2/s), Δc is the difference in CO_2 concentration across the sample (mol/m^3), and L is the sample length (m). The rate is obtained from the volumetric flow rate by reducing to standard pressure and temperature conditions and dividing by the volume of 1 mole of gas at STP (22.4 L).

The concentration Δc of CO_2 in the upstream reservoir is given by Henry's law with the Henry coefficient for CO_2 being 34 mol · m^{-3} · atm^{-1}. Since the sample area and length are known, D_e for the Carmel sample was calculated to be 6.3E−11 ± 0.32E−11 m^2/s.

3.2. Small-Angle and Very Small Angle Neutron Scattering

Combining small-angle (SANS) and very small angle (VSANS) neutron scattering provides nondestructive information on the pore space of micrometer- to nanometer-sized pore systems, such as in mudrocks. It has the advantage that the method requires relatively small sample volumes, in our case about 20 × 20 × 0.2 mm, which is a volume that is still considered to be representative for mudrocks when considering porosity or pore size characteristics, so a volume that is considerably larger than the representative elementary volume of mudrocks (up to lower
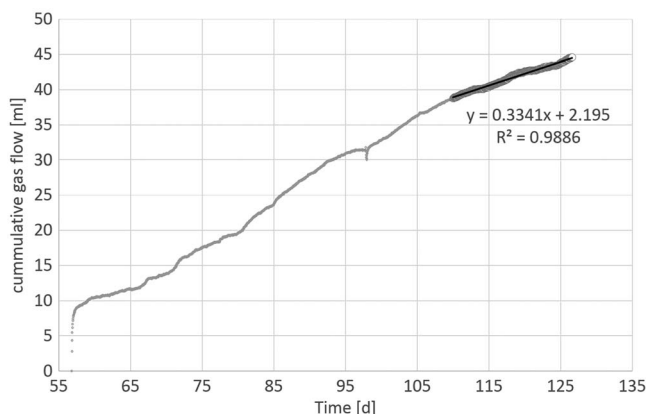
Figure 2. Cumulative CO_2 flow into Carmel sample under steady state conditions.

Plot shows: y = 0.3341x + 2.195, R^2 = 0.9886

micrometer range; Ma et al., 2017). A larger thickness might cause secondary scattering; a smaller thickness would lead to longer measurement times to obtain the same statistics in terms of total scatterers. Larger thicknesses might, however, be suitable for samples with a smaller pore density. The method provides information on fluid accessible and fluid nonaccessible pores; these can be differentiated by filling the pore space with deuterated water or deuterated methane and comparing with the air-filled measurement. Neutron scattering data provide important information on porosity, specific surface area, and pore size distribution, and depending on the instrument and instrument setting used, the pore size range can vary from 5 Å to 100 μm (Busch et al., 2017; Melnichenko, 2015). Despite the valuable data and information that can be gathered from such measurements, access to nuclear research facilities is limited to a few places worldwide only. This prohibits broad access to neutron scattering data and a comparison of statistically relevant datasets.

SANS experiments on Boom Clay were carried out using the General Purpose SANS (GP-SANS) instrument at Oak Ridge National Lab's High Flux Isotope Reactor facility, USA; SANS measurements on Carmel and Opalinus Shale samples were conducted at the KWS-1 instrument (Feoktystov et al., 2015; Frielinghaus et al., 2015) operated by the Jülich Centre for Neutron Science (JCNS) at Heinz Maier-Leibnitz Zentrum in Garching, Germany. All VSANS measurements were conducted at the KWS-3 instrument at JCNS (Pipich & Zhendong, 2015). Results for Opalinus Shale have been reported earlier (Busch et al., 2017). With the exception of one Boom Clay sample (K4), all samples were cut parallel to bedding, fixed on quartz glass carriers, and polished to a thickness of about 200 m. Samples were dried at room temperature, and measurements were performed under ambient pressure and temperature conditions.

In (V) SANS, a collimated neutron beam is elastically scattered by the sample (Guinier & Fournet, 1955; Radlinski, 2006). Position-sensitive detectors measure the scattering intensity $I(Q)$ as a function of the scattering angle, which is defined as the angular deviation from the incident beam. The momentum transfer Q (Å^{-1}) is related to the scattering angle θ by $Q = (4\pi/\lambda) \sin(\theta/2)$, where λ is the wavelength of the neutron beam. Thus, the size range of features accessible with neutron scattering depends on the neutron wavelength λ and the collected range of the scattering angle θ.

SANS data at KWS-1 (JCNS) were collected at a wavelength of λ of 6 Å. Measurements were performed at sample-to-detector distances of 1.2, 7.7, and 19.7 m, covering a Q-range of 0.002–0.35 Å^{-1}. The detector was a ^{6}Li glass scintillation detector with an active area of 60 × 60 cm^2. SANS data at GP-SANS (Oak Ridge National Lab) were measured at sample to detector distances of 1, 8, and 20 m. A neutron wavelength of 4.75 Å was selected for the short and medium distance, while 12-Å neutrons were used for measurements at the long sample-to-detector distance. These combined measurements cover a Q-range between 0.0008 and 0.8 Å^{-1}. Data at KWS-3 were collected at $\lambda = 12.8$ Å, $\Delta\lambda/\lambda = 0.16$, and a sample-to-detector distance of 9.5 m, covering a Q-range from 0.0024 to 0.00016 Å^{-1}. A ^{6}Li scintillation detector was used with a detector diameter of 9 cm. Hence, pore radii for the combined SANS and VSANS measurements range between $r \approx \pi/Q = 3$ Å and 1.5 μm. The data were corrected for background and empty slide scattering, detector pixel efficiency, and solid angle and normalized to transmission. Scattering was isotropic for all samples, and intensities were radially averaged to produce $I(Q)$ versus Q curves. The lower pore sizes were cut off at $Q = 0.2$ Å^{-1} or $r \sim 12.5$ Å during background subtraction to remove analytical artifacts arising from ordered stacking of clay minerals and errors from background values due to possible incoherent scattering on hydrogen atoms, which become significant at high Q.

The data processing and evaluation were carried out using the PRINSAS software (Hinde, 2004). The sensitivity to various input parameters and boundary conditions has been tested. Specific surface area and pore size distribution have been calculated for the entire sample set. In a first step, SANS data were entered into PRINSAS and displayed as I versus Q curves. Within the Porod limit, the curves are expected to be linear (on a log-log scale). Deviations from this linearity toward higher Q values indicate incoherent scattering background or presence of pores smaller than the cutoff range. A built-in routine can be used to determine the background by calculating the deviation of the last defined data point (set Q range) from the regression of the linear part of the curve. Background-corrected SANS data were merged with VSANS data by matching VSANS range intensities to the corresponding SANS data in the overlap region (Hinde, 2004). The PRINSAS model assumes spherical pore geometries, which is a simplification of the real geometries. Pores can be spherical, slit-shaped, or ellipsoidal or have more complex geometries, as has been shown in previous studies (Desbois et al., 2009; Leu et al., 2016; Loucks et al., 2009). We have used the spherical model in a previous

study on Opalinus Shale and demonstrated that porosity calculations originating from this approach match porosity determinations using Helium pycnometry or water porosimetry (Busch et al., 2017). Furthermore, using a different approach (e.g., ellipsoid pores) would not have an impact on the fractal dimension or the slope of the scattering intensity versus pore radius and we are therefore confident that the approach used in this study is suitable. Details on the calculation steps to obtain pore volume, specific surface area, and pore size distribution have been described previously (Busch et al., 2017; Kampman et al., 2016).

4. Fractal Model for the Prediction of Effective Diffusion Coefficients From Scattering Data

The surface fractal dimension D_s measures the roughness or tortuosity τ of a line or plane. A line embedded in a plane results in values for D_s between 1 (topological dimension of a straight line; $\tau = 1$) and 2 (topological dimension of a plane) and can be as high as 3 when embedded in a volume. In relation to the pore system of sedimentary rocks, D_s increases with any irregularity introduced at the solid/pore interface, and especially when these irregularities occur at increasingly fine scales (Mandelbrot, 1982). In the past, various studies have examined surface fractal dimensions in soils and its relationship to the tortuosity of pore networks or fractures (Ahl & Niemeyer, 1989; Young & Crawford, 1992). The volume (or mass) fractal dimension D_v in sedimentary rocks describes the heterogeneity and spatial occupation of pore volumes in a 3-D object. Volume fractals are directly related to the mass fractals, that is, the space within the object not filled by pores, but by mineral grains. The value of D_v is always <3 since it needs to be smaller than the embedding volume, which has a dimensionality of 3 (Anderson et al., 1996).

The fractal model used here is based on a scaling law developed previously (Gimenez et al., 1997; Liu et al., 2004; Liu & Nie, 2001), utilizing Archie's law for its derivation. The model relates the pore surface fractal dimension to the effective mean path length of a diffusing particle and the grain volume fractal to the effective porosity along the diffusing path. Since these parameters are accessible with small-angle scattering measurements, the model affords a method for relating the transport properties to SANS measurements.

The effective diffusion coefficient is directly related to the geometric factor G and the effective porosity ϕ_e by

$$D_e = \frac{D_{aq}\phi_e}{G}, \tag{5}$$

with D_{aq} the aqueous diffusion coefficient. Since the experiments involved in this study use fully water or gas saturated experiments, the effective porosity equals the total porosity φ_{tot}. Although the geometric factor is a fitting parameter, it is often written as

$$G = \frac{\tau}{\delta} \tag{6}$$

with the tortuosity τ [−] defined as the square of the ratio of the effective mean path length l_e of a diffusing particle to the linear distance l between beginning and end of the path (Epstein, 1989; Grathwohl, 1998):

$$\tau = \left(\frac{l_e}{l}\right)^2 \tag{7}$$

and constrictivity δ [−], which accounts for the reduction of the effective diffusion coefficient due to drag at the pore walls. It depends on the ratio of the solute diameter to the pore diameter (Grathwohl, 1998). It is assumed here that the constrictivity term equals one because the pore sizes probed are significantly larger than the molecule diameters of the gas species analyzed. This leads to

$$D_{eff} = \phi_e \frac{D_{aq}}{\tau} \tag{8}$$

According to Archie's law (Archie, 1942)

$$D_{eff} = D_{aq}\phi_e{}^m \tag{9}$$

where m [−] is the cementation factor. The applicability of Archie's law to model diffusion has been described in Van Loon and Mibus (2015). Comparison of (8) and (9) leads to a relationship between tortuosity and porosity:

$$\tau = \phi_e^{1-m} \tag{10}$$

The porosity follows from the scaling relationship between pore size and the grain volume fractal dimension as (Katz & Thompson, 1985):

$$\phi_e = \left(\frac{l_1}{l_2}\right)^{3-D_v} \tag{11}$$

where l_1 is the lower limit of the self-similar region, l_2 the upper limit, and D_v the fractal dimension of the pore solid interface. The upper limit l_2 is defined as the largest pore or grain and the lower cutoff as the smallest building block (e.g., an atom or molecule), that is, the smallest measurable pore. In our case, l_2 is the largest measurable pore size (3 μm) and l_1 the limit where the SANS curve is cut off to eliminate artifacts from incoherent scattering (12.5 Å). Expression (12) can be rewritten as

$$\frac{l_2}{l_1} = \phi_e^{-\frac{1}{3-D_v}} \tag{12}$$

According to Liu et al. (2004),

$$I = \left(\frac{l_2}{l_1}\right)^2 \tag{13}$$

and

$$I_e = \left(\frac{l_2}{l_1}\right)^{D_s} \tag{14}$$

where D_s is the surface fractal dimension. Substituting expressions (13) and (14) in expression (7) gives

$$\tau = \left(\frac{I_e}{I}\right)^2 = \left(\frac{l_2}{l_1}\right)^{2 D_s - 4} \tag{15}$$

Combining expressions (12) and (15) leads to

$$\tau = \phi_e^{\frac{2(2-D_s)}{3-D_v}} \tag{16}$$

and considering expression (10)

$$m = 1 + \frac{2(D_s - 2)}{3 - D_v} \tag{17}$$

5. Results and Discussion

The surface fractal dimension D_s can be obtained directly from the log-log plot of scattering intensity ($I(Q)$) versus momentum transfer (Q), which is he exponent C in the power law fit. The volume fractal dimension is derived from a pore frequency distribution f (r) versus pore radius plot (Figure 3); see, for example, Hinde (2004) for further details on the pore frequency distribution. The power law exponent in the I-Q curve typically has a value close to 3 but ranges from $3 < C < 4$. In a polydisperse system, $D_s = C - 1$ (Cherny et al., 2017; Martin, 1986). All fractal dimensions, as well as the scaling exponent m derived from SANS/VSANS data, are summarized in Table 4. Figure 4 shows a comparison for surface and volume fractal dimensions for the samples studied here and values provided by Liu et al. (2004). Note that D_s values generally decrease with an increase in D_v and show a similar behavior to those summarized previously (Liu et al., 2004).

The fractal dimensions are used to calculate the exponent m (equation (17)), providing values between 2.16 and 2.60 for Boom Clay, 2.04 for the Carmel sample, and 2.29–3.13 for the Opalinus Shale samples (Table 2).
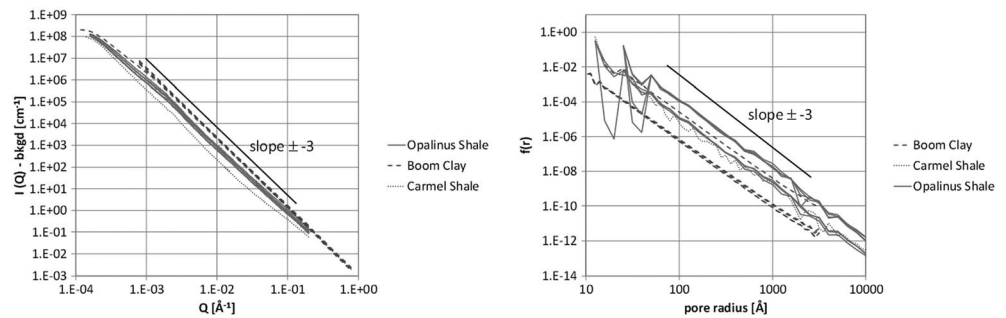
Figure 3. Log-log plots of the background-subtracted I-Q curves of (left) the combined SANS and VSANS data and (right) pore frequency distribution versus pore radius for Carmel, Opalinus, and Boom Clay samples. The slope of the curves is used to calculate the pore surface D_s and the pore volume D_v fractals and is ~3 for all samples.

Calculation of effective diffusion coefficients from this exponent to compare with experimental values requires knowledge of total porosity. For Carmel and Opalinus samples we used the porosity values obtained from (V) SANS data in earlier work (Busch et al., 2017; Kampman et al., 2016). The same approach to determine porosity for Boom Clay samples from scattering data was used in this study, resulting in porosity values between 13 and 30%. These porosities are lower than those reported in the literature, which range between 34 and 40% on the same samples. The reason for this difference is that Boom Clay holds quite significant amounts of porosity in pore sizes >1 μm (Hemes et al., 2015). This is not the case for Opalinus Shale as has been discussed earlier (Busch et al., 2017), and no reference values are available for the Carmel sample. These porosity differences are taken into consideration when presenting the comparison data between calculated and measured diffusion values below. Diffusive transport in clay interlayers is also neglected (e.g., Appelo et al., 2010). Aqueous diffusion coefficients of the different species were calculated following available models (Boudreau, 1997).

Comparison of the fractal-based diffusion coefficients with experimentally determined D_e in Figure 5 and Table 5 reveals a good agreement between the two values. All values are tabulated in Figure 5. All deviations are smaller than factor 5 for D_e values varying over 1.5 orders of magnitude. Note that no difference in matching the experimental values exists for samples cut parallel compared to perpendicular to bedding. All neutron scattering measurements were performed on samples cut parallel to bedding, that is, when the neutron beam hits the samples perpendicular to bedding. In plug-scale laboratory experiments, diffusive transport perpendicular to bedding reflects a harmonic averaging of effective diffusivities of individual laminae, whereas the neutron scattering measurements more closely approximate a volume weighted average. This may be a source of the small systematic difference between parallel versus perpendicular samples.

For Boom Clay samples, different diffusion coefficients were measured for different gas species, as well as different subsamples. Figure 5 shows that the modeled diffusion coefficients slightly underpredict the measured values when using porosities from SANS and slightly overpredict the measured values when using porosities provided by Jacops et al. (2017). For these samples, differences between diffusion coefficients measured perpendicular and parallel to bedding are similar, and the diffusing species has a larger control on the difference between measured and fractal model-derived D_e values. We speculate that the low anisotropy of Boom Clay results from its immaturity and the limited level of compaction and diagenesis. If there is a larger discrepancy for other types of mudrocks, maybe those that experience a higher degree of compaction remain to be tested. As a consequence, anisotropy is relatively small when comparing diffusion between parallel and perpendicular to bedding. Additionally, the diffusing species has a small, yet obvious impact on the quality of the reproducibility of the experimental data

Table 4

Surface and Volume Fractals Used for the Calculation of Effective Diffusion Coefficients and Tortuosity

	Sample orientation to bedding	D_s	D_v	m
Boom Clay				
K2	∥	2.141	2.824	2.602
K9	∥	2.133	2.743	2.035
K10	∥	2.216	2.643	2.210
K11	∥	2.192	2.672	2.171
K4	⊥	2.135	2.768	2.164
Carmel Claystone				
Carmel	∥	2.142	2.728	2.044
Opalinus Shale				
CCP1	∥	2.173	2.817	2.891
CCP4	∥	2.214	2.752	2.726
CCP5	∥	2.257	2.681	2.612
CCP6	∥	2.159	2.808	2.656
CCP7	∥	2.146	2.862	3.116
CCP9	∥	2.047	2.927	2.287
CCP12	∥	2.114	2.893	3.131
CCP14	∥	2.200	2.811	3.116
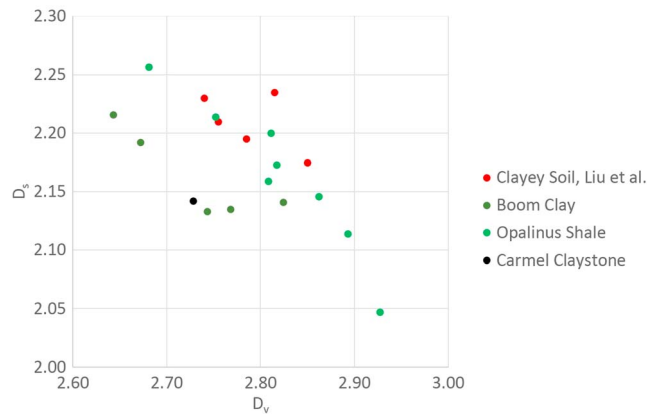
Figure 4. D_s versus D_v values for the three data sets investigated in this study and compared to values provided by Liu et al. (2004) for clayey soils.

using the fractal model. While the fit for CH_4 is marginally better than for HTO and H_2, the difference is small and the fit is markedly good for all species.

The Carmel sample shows slightly lower modeled versus measured effective diffusivity. The difference might be caused by a small underestimation of porosity, but we lack a large number of reference values due to the limited availability of the sample material.

For Opalinus Shale, measured D_e and fractal-based diffusivity show good agreement, although the fractal-based diffusivity has marginally higher values. Very good agreement of SANS-derived porosities with values obtained from other methods (such as helium pycnometry or water porosimetry) was found. It should be noted here that for Opalinus Shale a significant anisotropy has been determined for samples cut parallel compared to perpendicular to bedding (Van Loon et al., 2004). In this study we only compared with the parallel to bedding samples. This anisotropy can be more than 1 order of magnitude, demonstrating that orientation is important and sample orientation should be chosen with great care when selecting samples for SANS measurements. Since laboratory measurements of heterogeneous samples perpendicular to bedding reflect a harmonic averaging of diffusivity in contrasting layers, while the neutron scattering measurements reflect a volume weighted average, care should be taken when assessing the applicability of the scattering method to layer perpendicular measurements.

All laboratory diffusion tests have been performed on sample plugs saturated with aqueous solutions of different total salinity reflecting the original pore water (~1.18 g/L for Boom Clay, ~5 g/L for Carmel, and ~9.4 g/L for Opalinus). While the formulation we used to estimate bulk aqueous diffusion coefficients (Boudreau, 1997), used in the calculation of effective diffusivities, is independent of salinity, there is some experimental evidence that suggests that this may not be the case and that bulk aqueous CO_2 diffusion coefficients might, for instance, decrease by a factor 1.7 when increasing the salinity from 0 to 350 g/L NaCl (Belgodere et al., 2015). The maximum salinity used in this study is, however, 9.4 g/L, which would result in a decrease in aqueous diffusion coefficient that is marginal, and this effect can therefore be neglected.
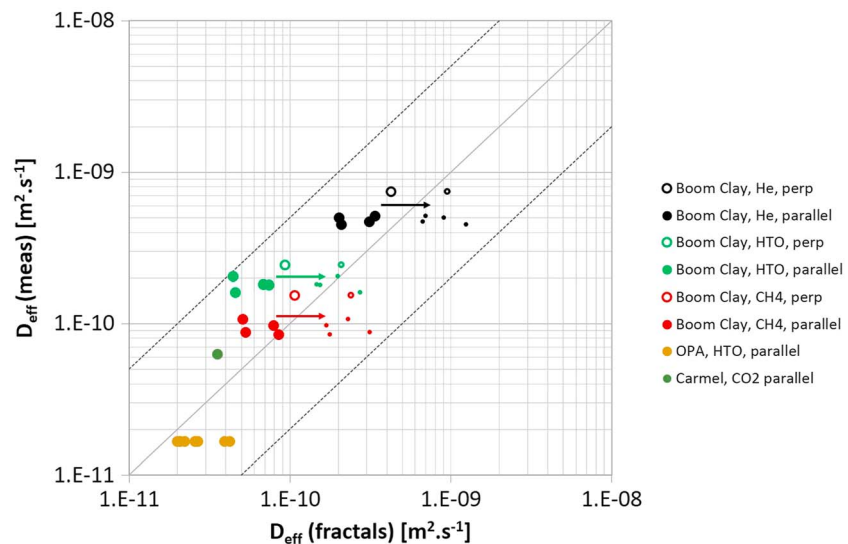
Figure 5. Measured versus modeled effective diffusion coefficients for the three different sample sets used in this study. For Boom Clay, the large symbols relate to calculated diffusion coefficients based on SANS porosity, the small symbols to those using porosities from Jacops et al. (2017). Dashed lines represent factors 5 higher or lower than the 1:1 line.

Table 5
Summary of Diffusion Coefficients Calculated Using the Fractal Model and Experimentally Obtained on Plug Samples

	Solute	D_{aq} (m^2/s)	Φ (−)	Fractal model τ	Fractal model D_e (m^2/s)	Experimental D_e (m^2/s)
Boom Clay						
K2	He	7.3E−09	0.30	6.9574	3.1E−10	4.7E−10
K9	He	7.3E−09	0.17	6.0847	2.1E−10	4.5E−10
K10	He	7.3E−09	0.20	7.1278	2.0E−10	5.0E−10
K11	He	7.3E−09	0.24	5.2420	3.4E−10	5.1E−10
K4	He	7.3E−09	0.27	4.6295	4.2E−10	7.5E−10
K2	CH4	1.8E−09	0.30	6.9574	7.9E−11	9.7E−11
K9	CH4	1.8E−09	0.17	6.0847	5.3E−11	8.8E−11
K10	CH4	1.8E−09	0.20	7.1278	5.1E−11	1.1E−10
K11	CH4	1.8E−09	0.24	5.2420	8.5E−11	8.4E−11
K4	CH4	1.8E−09	0.27	4.6295	1.1E−10	1.6E−10
K2	HTO	1.6E−09	0.30	6.9574	6.9E−11	1.8E−10
K9	HTO	1.6E−09	0.17	6.0847	4.6E−11	1.6E−10
K10	HTO	1.6E−09	0.20	7.1278	4.4E−11	2.1E−10
K11	HTO	1.6E−09	0.24	5.2420	7.4E−11	1.8E−10
K4	HTO	1.6E−09	0.27	4.6295	9.3E−11	2.5E−10
Carmel Claystone						
Carmel	CO2	2.45E−09	0.13	8.71	3.5E−11	6.3E−11
Opalinus Shale						
CCP1	HTO	1.60E−09	0.23	16.4753	2.2E−11	5.4E−11
CCP4	HTO	1.60E−09	0.20	15.6732	2.1E−11	5.4E−11
CCP5	HTO	1.60E−09	0.25	9.4208	4.2E−11	5.4E−11
CCP6	HTO	1.60E−09	0.19	15.0950	2.1E−11	5.4E−11
CCP7	HTO	1.60E−09	0.27	16.0750	2.7E−11	5.4E−11
CCP9	HTO	1.60E−09	0.20	8.0759	3.9E−11	5.4E−11
CCP12	HTO	1.60E−09	0.25	19.8377	2.0E−11	5.4E−11
CCP14	HTO	1.60E−09	0.27	16.5682	2.6E−11	5.4E−11

Note. Experimental Boom Clay values from Jacops et al. (2017), Opalinus Shale values from Pearson et al. (2003), and Carmel value from this study.

6. Conclusions

This study provides, for the first time, experimental verification of a fractal diffusion model in mudrocks. This study demonstrates that the complete pore network characterization, from nanometers to micron scales, can be performed using small-angle scattering techniques, which provides measurements of the fractal dimensions, porosities, surface areas, etc., even for samples with very low porosities.

Effective diffusion coefficients were calculated from SANS pore network characterization using a fractal model (Liu et al., 2004). Verification of the model is obtained by comparison to experimental measurements, using the same samples (Carmel and Boom Clay) or samples from the same location and sedimentary facies (Opalinus Shale).

The agreement between measured and modeled D_e values for samples cut parallel to bedding is good, with deviations between the two techniques being generally less than factor 5. For samples cut perpendicular to bedding a systematic offset in the agreement between measured and modeled data is observed, meaning that all measured data have higher D_e than the corresponding calculated data. We posit that this is because in plug-scale laboratory measurements, diffusive transport perpendicular to bedding reflects a harmonic averaging of effective diffusivities of individual laminae (layers of different mineralogy and pore size distribution), weighting layers with the lowest effective diffusivities, whereas the neutron scattering measurements more closely approximate a volume-weighted average. In general, diffusion is more rapid parallel rather than perpendicular to bedding due to anisotropy in pore connectivity and the high sensitivity of layer-perpendicular diffusion to layers with low effective diffusivity.

We conclude that laboratory diffusion measurements are the most reliable method to obtain effective diffusion coefficients for low-permeability rocks. However, small-angle neutron scattering measurements provide a

reliable method to retrieve not only effective diffusion coefficients but also simultaneously a suit of parameters (porosity, pore surface areas, and pore size distributions) important for (reactive) transport modeling. The technique enables measurements at different scales and orientations, thus allowing the relationship of these transport properties to other rock properties, such as mineralogy or mechanical properties, to be investigated further.

References

Ahl, C., & Niemeyer, J. (1989). The fractal dimension of the pore-volume inside soils. *Zeitschrift für Pflanzenernährung und Bodenkunde*, *152*(5), 457–458. https://doi.org/10.1002/jpln.19891520512

Altmann, S., Tournassat, C., Goutelard, F., Parneix, J.-C., Gimmi, T., & Maes, N. (2012). Diffusion-driven transport in clayrock formations. *Applied Geochemistry*, *27*(2), 463–478. https://doi.org/10.1016/j.apgeochem.2011.09.015

Anderson, A. N., Crawford, J. W., & McBratney, A. B. (2000). On diffusion in fractal soil structures. *Soil Science Society of America Journal*, *64*(1), 19–24. https://doi.org/10.2136/sssaj2000.64119x

Anderson, A. N., McBratney, A. B., & FitzPatrick, E. A. (1996). Soil mass, surface, and spectral fractal dimensions estimated from thin section photographs. *Soil Science Society of America Journal*, *60*(4), 962–969. https://doi.org/10.2136/sssaj1996.0361599 5006000040002x

Appelo, C., Van Loon, L., & Wersin, P. (2010). Multicomponent diffusion of a suite of tracers (HTO, Cl, Br, I, Na, Sr, Cs) in a single sample of Opalinus Clay. *Geochimica et Cosmochimica Acta*, *74*(4), 1201–1219.

Archie, G. E. (1942). The electrical resistivity log as an aid in determining some reservoir characteristics. *Transactions of AIME*, *146*(01), 54–62. https://doi.org/10.2118/942054-G

Backeberg, N. R., Iacoviello, F., Rittner, M., Mitchell, T. M., Jones, A. P., Day, R., et al. (2017). Quantifying the anisotropy and tortuosity of permeable pathways in clay-rich mudstones using models based on X-ray tomography. *Scientific Reports*, *7*(1), 14838. https://doi.org/10.1038/s41598-017-14810-1

Beerten, K., De Craen, M., & Wouters, L. (2013). Patterns and estimates of post-Rupelian burial and erosion in the Campine area, north-eastern Belgium. *Physics and Chemistry of the Earth, Parts A/B/C*, *64*, 12–20. https://doi.org/10.1016/j.pce.2013.04.003

Belgodere, C., Dubessy, J., Vautrin, D., Caumon, M.-C., Sterpenich, J., Pironon, J., et al. (2015). Experimental determination of CO2 diffusion coefficient in aqueous solutions under pressure at room temperature via Raman spectroscopy: Impact of salinity (NaCl). *Journal of Raman Spectroscopy*, *46*(10), 1025–1032. https://doi.org/10.1002/jrs.4742

Blakey, R. C., Havholm, K. G., & Jones, L. S. (1996). Stratigraphic analysis of eolian interactions with marine and fluvial deposits, Middle Jurassic Page Sandstone and Carmel Formation, Colorado Plateau, USA. *Journal of Sedimentary Research*, *66*(2), 324–342.

Bossart, P., & Thury, M. (2008). Mont Terri rock laboratory—Project, programme 1996 to 2007 and results Rep., Federal Office of Topology Swisstopo.

Boudreau, B. P. (1997). *Diagenetic models and their implementation—Modelling transport and reactions in aquatic sediments*. Berlin: Springer. https://doi.org/10.1007/978-3-642-60421-8

Busch, A., Alles, S., Gensterblum, Y., Prinz, D., Dewhurst, D. N., Raven, M. D., et al. (2008). Carbon dioxide storage potential of shales. *International Journal of Greenhouse Gas Control*, *2*(3), 297–308. https://doi.org/10.1016/j.ijggc.2008.03.003

Busch, A., Schweinar, K., Kampman, N., Coorn, A., Pipich, V., Feoktystov, A., et al. (2017). Determining the porosity of mudrocks using methodological pluralism. *Geological Society, London, Special Publications*, *454*(1), 15–38. https://doi.org/10.1144/sp454.1

Cherny, A. Y., Anitas, E. M., Osipov, V. A., & Kuklin, A. I. (2017). Scattering from surface fractals in terms of composing mass fractals. *Journal of Applied Crystallography*, *50*(3), 919–931. https://doi.org/10.1107/S1600576717005696

Crawford, J. W., & Matsui, N. (1996). Heterogeneity of the pore and solid volume of soil: Distinguishing a fractal space from its non-fractal complement. *Geoderma*, *73*(3–4), 183–195. https://doi.org/10.1016/0016-7061(96)00045-6

Crawford, J. W., Ritz, K., & Young, I. M. (1993). Quantification of fungal morphology, gaseous transport and microbial dynamics in soil: An integrated framework utilising fractal geometry. *Geoderma*, *56*(1), 157–172. https://doi.org/10.1016/0016-7061(93)90107-V

Cui, X., Bustin, A., & Bustin, R. M. (2009). Measurements of gas permeability and diffusivity of tight reservoir rocks: Different approaches and their applications. *Geofluids*, *9*(3), 208–223. https://doi.org/10.1111/j.1468-8123.2009.00244.x

De Craen, M., Wang, L., Van Geet, M., & Moors, H. (2004). Geochemistry of Boom Clay pore water at the Mol site. SCK-CEN BLG-990*Rep. SCK-CEN BLG-990*, Mol, Belgium.

Desbois, G., Urai, J. L., & Kukla, P. A. (2009). Morphology of the pore space in claystones—Evidence from BIB/FIB ion beam sectioning and cryo-SEM observations. *Earth Discussions*, *4*(1), 15–22. https://doi.org/10.5194/ee-4-15-2009

Epstein, N. (1989). On tortuosity and the tortuosity factor in flow and diffusion through porous media. *Chemical Engineering Science*, *44*(3), 777–779. https://doi.org/10.1016/0009-2509(89)85053-5

Falconer, K. (2004). *Fractal geometry: Mathematical foundations and applications*. John Wiley & Sons.

Feoktystov, A. V., Frielinghaus, H., di, Z., Jaksch, S., Pipich, V., Appavou, M. S., et al. (2015). KWS-1 high-resolution small-angle neutron scattering instrument at JCNS: Current state. *Journal of Applied Crystallography*, *48*(1), 61–70. https://doi.org/10.1107/S1600576714025977

Frielinghaus, H., Feoktystov, A., Berts, I., & Mangiapia, G. (2015). KWS-1: Small-angle scattering diractometer. *Journal of Large-Scale Research Facilities*, *1*(A28), 1–4.

Ghanbarian, B., Hunt, A. G., Skaggs, T. H., & Jarvis, N. (2017). Upscaling soil saturated hydraulic conductivity from pore throat characteristics. *Advances in Water Resources*, *104*, 105–113. https://doi.org/10.1016/j.advwatres.2017.03.016

Gimenez, D., Perfect, E., Rawls, W. J., & Pachepsky, Y. (1997). Fractal models for predicting soil hydraulic properties: A review. *Engineering Geology*, *48*(3-4), 161–183. https://doi.org/10.1016/S0013-7952(97)00038-0

Grathwohl, P. (1998). *Diffusion in natural porous media: Contaminant transport, sorption/desorption and dissolution kinetics*. US: Springer.

Guinier, A., & Fournet, G. (1955). *Small-angle scattering of X-rays* (p. 268). New York: John Wiley.

Hemes, S., Desbois, G., Urai, J. L., Schröppel, B., & Schwarz, J.-O. (2015). Multi-scale characterization of porosity in Boom Clay (HADES-level, Mol, Belgium) using a combination of X-ray μ-CT, 2D BIB-SEM and FIB-SEM tomography. *Microporous and Mesoporous Materials*, *208*(0), 1–20. https://doi.org/10.1016/j.micromeso.2015.01.022

Hinde, A. (2004). PRINSAS—A Windows-based computer program for the processing and interpretation of small-angle scattering data tailored to the analysis of sedimentary rocks. *Journal of Applied Crystallography*, *37*(6), 1020–1024. https://doi.org/10.1107/S0021889804021260

Jacops, E., Aertsens, M., Maes, N., Bruggeman, C., Krooss, B. M., Amann-Hildenbrand, A., et al. (2017). Interplay of molecular size and pore network geometry on the diffusion of dissolved gases and HTO in Boom Clay. *Applied Geochemistry*, *76*, 182–195. https://doi.org/10.1016/j.apgeochem.2016.11.022

Jacops, E., Maes, T., Maes, N., Volckaert, G., Weetjens, E., & Sillen, X. (2015a). Gas-driven radionuclide transport in undisturbed and disturbed Boom Clay. *Geological Society, London, Special Publications*, *415*(1), 9–17. https://doi.org/10.1144/sp415.10

Jacops, E., Volckaert, G., Maes, N., Weetjens, E., & Govaerts, J. (2013). Determination of gas diffusion coefficients in saturated porous media: He and CH_4 diffusion in Boom Clay. *Applied Clay Science*, *83-84*, 217–223. https://doi.org/10.1016/j.clay.2013.08.047

Jacops, E., Wouters, K., Volckaert, G., Moors, H., Maes, N., Bruggeman, C., et al. (2015b). Measuring the effective diffusion coefficient of dissolved hydrogen in saturated boom clay. *Applied Geochemistry*, *61*(0), 175–184. https://doi.org/10.1016/j.apgeochem.2015.05.022

Kampman, N., Bickle, M. J., Maskell, A., Chapman, H. J., Evans, J. P., Purser, G., et al. (2014). Drilling and sampling a natural CO_2 reservoir: Implications for fluid flow and CO_2-fluid-rock reactions during CO_2 migration through the overburden. *Chemical Geology*, *369*(0), 51–82. https://doi.org/10.1016/j.chemgeo.2013.11.015

Kampman, N., Busch, A., Bertier, P., Snippe, J., Hangx, S., Pipich, V., et al. (2016). Observational evidence confirms modelling of the long-term integrity of CO_2-reservoir caprocks. *Nature Communications*, *7*. https://doi.org/10.1038/ncomms12268

Kampman, N., Maskell, A., Bickle, M. J., Evans, J. P., Schaller, M., Purser, G., et al. (2013). Scientific drilling and downhole fluid sampling of a natural CO_2 reservoir, Green River, Utah. *Scientific Drilling*, *16*, 33–43. https://doi.org/10.5194/sd-16-33-2013

Katz, A. J., & Thompson, A. H. (1985). Fractal sandstone pores: Implications for conductivity and pore formation. *Physical Review Letters*, *54*(12), 1325–1328. https://doi.org/10.1103/PhysRevLett.54.1325

Keller, L. M., Schuetz, P., Erni, R., Rossell, M. D., Lucas, F., Gasser, P., & Holzer, L. (2013). Characterization of multi-scale microstructural features in Opalinus Clay. *Microporous and Mesoporous Materials*, *170*, 83–94. https://doi.org/10.1016/j.micromeso.2012.11.029

Krohn, C. E. (1988). Fractal measurements of sandstones, shales, and carbonates. *Journal of Geophysical Research*, *93*(B4), 3297–3305. https://doi.org/10.1029/JB093iB04p03297

Krooss, B., & Schaefer, R. G. (1987). Experimental measurements of the diffusion parameters of light hydrocarbons in water-saturated sedimentary rocks: I. A new experimental procedure. *Organic Geochemistry*, *11*(3), 193–199. https://doi.org/10.1016/0146-6380(87)90022-2

Krooss, B. M. (1988). Experimental investigation of the molecular migration of C1-C6 hydrocarbons: Kinetics of hydrocarbon release from source rocks. *Organic Geochemistry*, *13*(1–3), 513–523. https://doi.org/10.1016/0146-6380(88)90072-1

Leu, L., Georgiadis, A., Blunt, M. J., Busch, A., Bertier, P., Schweinar, K., et al. (2016). Multiscale description of shale pore systems by scanning SAXS and WAXS microscopy. *Energy & Fuels*, *30*(12), 10,282–10,297. https://doi.org/10.1021/acs.energyfuels.6b02256

Leythaeuser, D., Schaefer, R. G., & Yukler, A. (1980). Diffusion of light hydrocarbons through near-surface rocks. *Nature*, *284*(5756), 522–525. https://doi.org/10.1038/284522a0

Liu, H., Zhang, Y., Zhou, Q., & Molz, F. (2007). An interpretation of potential scale dependence of the effective matrix diffusion coefficient. *Journal of Contaminant Hydrology*, *90*(1–2), 41–57. https://doi.org/10.1016/j.jconhyd.2006.09.006

Liu, J.-G., & Nie, Y.-F. (2001). Fractal scaling of effective diffusion coefficient of solute in porous media. *Journal of Environmental Sciences*, *13*(2), 170–172.

Liu, J.-G., Wang, H.-T., & Nie, Y.-F. (2004). Fractal model for predicting effective diffusion coefficient of solute in porous media. *Advances in Water Science*, *15*(4), 458–462.

Loucks, R. G., Reed, R. M., Ruppel, S. C., & Jarvie, D. M. (2009). Morphology, genesis, and distribution of nanometer-scale pores in siliceous mudstones of the Mississippian Barnett Shale. *Journal of Sedimentary Research*, *79*(12), 848–861. https://doi.org/10.2110/jsr.2009.092

Ma, L., Fauchille, A.-L., Dowey, P. J., Figueroa Pilz, F., Courtois, L., Taylor, K. G., & Lee, P. D. (2017). Correlative multi-scale imaging of shales: A review and future perspectives. *Geological Society, London, Special Publications*, *454*(1), 175–199. https://doi.org/10.1144/sp454.11

Maes, N., Salah, S., Jacques, D., Aertsens, M., Van Gompel, M., De Cannière, P., & Velitchkova, N. (2008). Retention of Cs in Boom Clay: Comparison of data from batch sorption tests and diffusion experiments on intact clay cores. *Physics and Chemistry of the Earth, Parts A/B/C*, *33*(Supplement 1), S149–S155. https://doi.org/10.1016/j.pce.2008.10.002

Maes, N., Wang, L., Delecaut, G., Van Geet, M., Put, M., Weetjens, E., et al. (2004). Migration case study: Transport of radionuclides in a reducing clay sediment (TRANCOM 2) contract no FIKW-CT-2000-00008*Rep. EUR-21022*, Luxembourg.

Mandelbrot, B. B. (1982). *The fractal geometry of nature*. San Francisco, USA: Freeman.

Martin, J. (1986). Scattering exponents for polydisperse surface and mass fractals. *Journal of Applied Crystallography*, *19*(1), 25–27. https://doi.org/10.1107/S0021889886090052

Meakin, P. (1991). Fractal aggregates in geophysics. *Reviews of Geophysics*, *29*(3), 317–354. https://doi.org/10.1029/91RG00688

Melnichenko, Y. B. (2015). *Small-angle scattering from confined and interfacial fluids*. Cham: Springer.

Pearson, F. J., Arcos, D., Bath, A., Boisson, J.-Y., Fernández, A. M., Gäbler, H.-E., et al. (2003). Mont Terri project—Geochemistry of water in the Opalinus Clay Formation at the Mont Terri rock laboratory, Berichte des BWG. *Serie Geologie*, *5*.

Pipich, V., & Zhendong, F. (2015). KWS-3: Very small angle scattering diffractometer with focusing mirror. *Journal of Large-Scale Research Facilities*, *1*, A31. https://doi.org/10.17815/jlsrf-1-28

Radlinski, A., & Hinde, A. (2002). Small angle neutron scattering and petroleum geology. *Neutron News*, *13*(2), 10–14. https://doi.org/10.1080/10448630208218477

Radlinski, A. P. (2006). Small-angle neutron scattering and the microstructure of rocks. *Reviews in Mineralogy and Geochemistry*, *63*(1), 363–397. https://doi.org/10.2138/rmg.2006.63.14

Radlinski, A. P., Radlinska, E. Z., Agamalian, M., Wignall, G. D., Lindner, P., & Randl, O. G. (1999). Fractal geometry of rocks. *Physical Review Letters*, *82*(15), 3,078–3,081. https://doi.org/10.1103/PhysRevLett.82.3078

Rebour, V., Billiotte, J., Deveughele, M., Jambon, A., & le Guen, C. (1997). Molecular diffusion in water-saturated rocks: A new experimental method. *Journal of Contaminant Hydrology*, *28*(1-2), 71–93. https://doi.org/10.1016/S0169-7722(96)00051-4

Rubel, A., Sonntag, C., Lippmann, J., Pearson, F., & Gautschi, A. (2002). Solute transport in formations of very low permeability: Profiles of stable isotope and dissolved noble gas contents of pore water in the Opalinus Clay, Mont Terri, Switzerland. *Geochimica et Cosmochimica Acta*, *66*(8), 1311–1321. https://doi.org/10.1016/s0016-7037(01)00859-6

Schlömer, S., & Krooss, B. M. (1997). Experimental characterisation of the hydrocarbon sealing efficiency of cap rocks. *Marine and Petroleum Geology*, *14*(5), 565–580. https://doi.org/10.1016/S0264-8172(97)00022-6

Schlömer, S., & Krooss, B. M. (2004). Molecular transport of methane, ethane nd nitrogene and the influence of diffusion on the chemical and isotopic composition of natural gas accumulations. *Geofluids*, *4*(1), 81–108. https://doi.org/10.1111/j.1468-8123.2004.00076.x

Seemann, T., Bertier, P., Krooss, B. M., & Stanjek, H. (2017). Water vapour sorption on mudrocks. *Geological Society, London, Special Publications*, *454*(1), 201–233. https://doi.org/10.1144/sp454.8

Stanjek, H., & Künkel, D. (2016). CEC determination with Cutriethylenetetramine: Recommendations for improving reproducibility and accuracy, 1–17 pp.

Sterling, M. C. Jr., Bonner, J. S., Ernest, A. N., Page, C. A., & Autenrieth, R. L. (2005). Application of fractal flocculation and vertical transport model to aquatic sol–sediment systems. *Water Research*, *39*(9), 1818–1830. https://doi.org/10.1016/j.watres.2005.02.007

Thompson, A. H. (1991). Fractals in rock physics. *Annual Review of Earth and Planetary Sciences*, *19*(1), 237–262. https://doi.org/10.1146/annurev.ea.19.050191.001321

Ufer, K., Stanjek, H., Roth, G., Dohrmann, R., Kleeberg, R., & Kaufhold, S. (2008). Quantitative phase analysis of bentonites by the Rietveld method. *Clays and Clay Minerals*, *56*(2), 272–282. https://doi.org/10.1346/ccmn.2008.0560210

Van Loon, L. R., & Mibus, J. (2015). A modified version of Archie's law to estimate effective diffusion coefficients of radionuclides in argillaceous rocks and its application in safety analysis studies. *Applied Geochemistry*, *59*, 85–94. https://doi.org/10.1016/j.apgeochem.2015.04.002

Van Loon, L. R., Soler, J. M., & Bradbury, M. H. (2003). Diffusion of HTO, 36Cl— and 125I— in Opalinus Clay samples from Mont Terri: Effect of confining pressure. *Journal of Contaminant Hydrology*, *61*(1–4), 73–83. https://doi.org/10.1016/S0169-7722(02)00114-6

Van Loon, L. R., Soler, J. M., Mueller, W., & Bradbury, M. H. (2004). Anisotropic diffusion in layered argillaceous rocks: A case study with Opalinus Clay. *Environmental Science & Technology*, *38*(21), 5721–5728. https://doi.org/10.1021/es049937g

Wentinck, H. M., & Busch, A. (2017). Modelling of CO_2 diffusion and related poro-elastic effects in a smectite-rich cap rock above a reservoir used for CO_2 storage. *Geological Society, London, Special Publications*, *454*(1), 155–173. https://doi.org/10.1144/sp454.4

Yang, F., Ning, Z. F., Wang, Q., Kong, D. T., Peng, K., & Xiao, L. F. (2014). Fractal characteristics of nanopore in shales. *Natural Gas Geoscience*, *25*(4), 618–623. https://doi.org/10.11764/j.issn.1672-1926.2014.04.0618

Young, I., & Crawford, J. (1992). The analysis of fracture profiles of soil using fractal geometry. *Soil Research*, *30*(3), 291–295. https://doi.org/10.1071/SR9920291

Yuan, W., Pan, Z., Li, X., Yang, Y., Zhao, C., Connell, L. D., et al. (2014). Experimental study and modelling of methane adsorption and diffusion in shale. *Fuel*, *117*(PART A), 509–519. https://doi.org/10.1016/j.fuel.2013.09.046

Zeelmaekers, E., Honty, M., Derkowski, A., Środoń, J., De Craen, M., Vandenberghe, N., et al. (2015). Qualitative and quantitative mineralogical composition of the Rupelian Boom Clay in Belgium. *Clay Minerals*, *50*(02), 249–272. https://doi.org/10.1180/claymin.2015.050.2.08

Zhang, R., Liu, S., & Wang, Y. (2017). Fractal evolution under in situ pressure and sorption conditions for coal and shale. *Scientific Reports*, *7*(1), 8971. https://doi.org/10.1038/s41598-017-09324-9